NANO LETTERS
Cite This: Nano Lett. 2019, 19, 770−774
Letter
pubs.acs.org/NanoLett

Spatial Separation of Carrier Spin by the Valley Hall Effect in Monolayer WSe_2 Transistors

Elyse Barré,[†] Jean Anne C. Incorvia,[†,‡] Suk Hyun Kim,[§] Connor J. McClellan,[†] Eric Pop,[†,∥] H.-S. Philip Wong,[†] and Tony F. Heinz*[,§,⊥]

[†]Department of Electrical Engineering, Stanford University, Stanford, California 94305, United States
[‡]Department of Electrical and Computer Engineering, University of Texas at Austin, Austin, Texas 78712, United States
[§]Departments of Applied Physics and Photon Science, Stanford University, Stanford, California 94305, United States
[∥]Department of Materials Science and Engineering, Stanford University, Stanford, California 94305, United States
[⊥]SLAC National Accelerator Laboratory, Menlo Park, California 94025, United States

Supporting Information

ABSTRACT: We investigate the valley Hall effect (VHE) in monolayer WSe_2 field-effect transistors using optical Kerr rotation measurements at 20 K. While studies of the VHE have so far focused on n-doped MoS_2, we observe the VHE in WSe_2 in both the n- and p-doping regimes. Hole doping enables access to the large spin-splitting of the valence band of this material. The Kerr rotation measurements probe the spatial distribution of the valley carrier imbalance induced by the VHE. Under current flow, we observe distinct spin-valley polarization along the edges of the transistor channel. From analysis of the magnitude of the Kerr rotation, we infer a spin-valley density of 44 spins/μm, integrated over the edge region in the p-doped regime. Assuming a spin diffusion length less than 0.1 μm, this corresponds to a spin-valley polarization of the holes exceeding 1%.

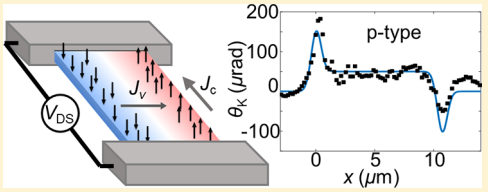

KEYWORDS: *Tungsten diselenide, magneto-optical Kerr effect, valleytronics, spintronics*

Ultrathin semiconducting transition metal dichalcogenides (TMDCs) have attracted attention for next-generation nanoelectronics because of their highly tunable optical and electronic properties.[1−4] They also have potential for spin- and valleytronics. In particular, with strong spin−orbit coupling and broken inversion symmetry at monolayer thickness, these materials are expected to exhibit a coupled spin and valley Hall effect (VHE).[5−7] The monolayer TMDCs feature nonzero Berry curvature, combined with a large (hundreds of meV) spin splitting, Δ_{SOC-p}, in the valence band and smaller spin splitting, Δ_{SOC-n}, in the conduction band at the K and K′ band extrema (Figure 1a). The Berry curvature and spin of carriers in the valence and conduction bands around the K and K′ points are equal in magnitude but opposite in sign.[6,7] In addition to its fundamental interest, the VHE in TMDCs could lead to novel device applications, such as an electrically gate-controlled method to switch nanomagnets for spintronics and memory.

Previous work has demonstrated the VHE in monolayer and bilayer n-doped MoS_2[5,8] through the observation of the spatial separation of carriers in the K and K′ valleys under current flow in the semiconductor. The present work complements these earlier studies by exploring the phenomenon in monolayer WSe_2 in both the n- and p-doped regimes. In WSe_2, both the valence and conduction band spin splitting are significant, 460 and 30 meV, respectively.[9−11] Thus, in our low-temperature measurements, the VHE carries spin along with the valley information for both electrons and holes. Because of the large spin splitting of the valence band, we expect that holes in a given valley retain their spin information even at room temperature. Thus, p-type TMDCs, including WSe_2, are promising candidates for spin-based applications at elevated temperatures. The large spin splitting also makes the VHE for holes more resistant to influence of magnetic fields and Rashba-related contributions to the Berry phase.[12,13]

For this work, we fabricated WSe_2 field-effect transistors (FETs) to measure the accumulation of valley and spin polarized carriers under different gating and bias conditions. Figure 1b,c illustrates, respectively, the transistor structure and the influence of the VHE when current flows through the channel. We control the transistor through its source-drain voltage V_{DS} (with source voltage as reference), which creates an in-plane electric field $E\hat{y}$ and charge (sheet) current density $J_D\hat{y}$ along the channel, and a back-gate voltage V_{GS}, which modulates the Fermi level in the WSe_2 channel. For appropriate bias voltages V_{DS} and V_{GS}, a spin-valley Hall current $J_v\hat{x}$ is generated perpendicular to the charge current across the sample. Note that no external magnetic field needs to be applied.

Optical Characterization of Valley Hall Effect. We probe the presence of valley- and spin- polarized carriers using the valley circular dichroism of the monolayer WSe_2 through

Received: September 21, 2018
Revised: December 19, 2018
Published: January 2, 2019

DOI: 10.1021/acs.nanolett.8b03838
Nano Lett. 2019, 19, 770−774

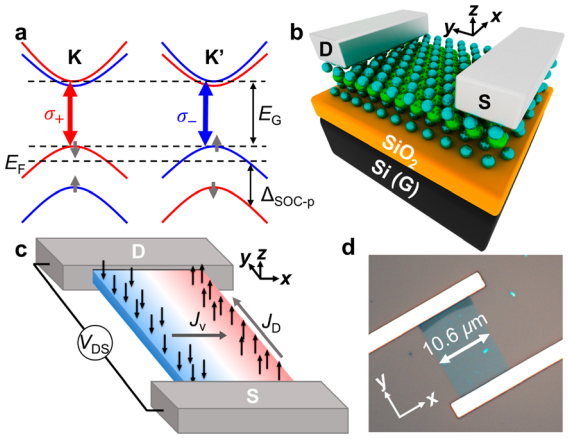

Figure 1. (a) Schematic of the band extrema at the K and K′ points in monolayer WSe_2. The figure shows the valence-band spin splitting Δ_{SOC-p} = 0.46 eV (the conduction splitting, Δ_{SOC-n} = 0.030 eV, is not labeled) and the allowed optical transitions for circularly polarized light. E_G is the band gap and E_F is a representative Fermi energy for a p-doped sample. Gray arrows show the spin nature of the valence levels. (b) Diagram of the fabricated monolayer WSe_2 transistor (not to scale). In the WSe_2 monolayer, the tungsten (W) atoms are shown in green and the selenium (Se) atoms in blue. Contacts for the source (S) and drain (D) are made with Pd films. The transistor structure uses a Si back-gate (in black, G) and a SiO_2 dielectric (orange) of 100 nm thickness. (c) Illustration of the VHE, showing the charge current density J_D and spin-valley current density J_v. The accumulation of spin-valley polarized carriers at the edges of the sample is shown with red and blue shading. (d) Microscope image of the sample, with monolayer WSe_2 in center and 30 nm thick Pd source and drain contacts. The device dimensions are 10.6 μm × 20 μm.

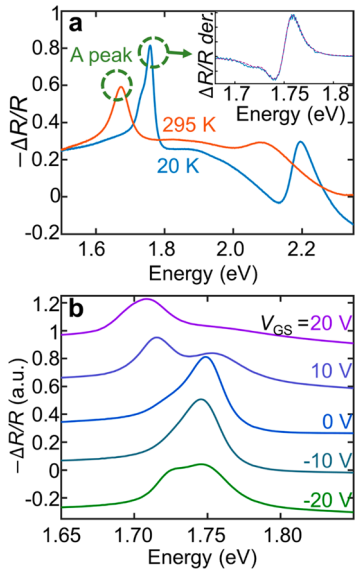

Figure 2. (a) Reflection contrast spectra of the device at room temperature and cooled with liquid helium for V_{GS} = 0 V, showing a large blue shift in energy and narrowing of excitonic peaks at low temperature. The inset shows a fit of A exciton peak (purple) to the first derivative of the reflection contrast spectrum (blue). (b) Reflection contrast spectra at 20 K for gate voltages V_{GS} varying from n- to p-doping. The curves are offset for clarity.

measurement of optical Kerr rotation (see Supporting Information Section S1 for measurement details). As shown in Figure 1a, light of σ+ ($\sigma-$) circular polarization selectively probes transitions in the K (K′) valley.[14,15] Thus, if the valley carrier populations are different, the dielectric function for the two circularly polarized states of light will also differ. Correspondingly, linearly polarized light will acquire a Kerr rotation (KR) angle, θ_K, in passing through or being reflected from the sample supported on a substrate.

An optical image of the device is shown in Figure 1d. We map the effect of the VHE by recording the KR with a tightly focused laser while rastering the sample in the transverse ($\hat{x}$) direction. The sample was supported on SiO_2 (100 nm) on a highly doped Si substrate, which served as our back-gate (see Supporting Information Section S2 for details about the device). We used gate voltages V_{GS} = −30 or 30 V with a sinusoidally varying drain voltage of V_{DS} = 5 V_P (peak voltage, in Volts) at frequencies from 200 to 800 Hz and detected synchronously the electric signal from the Kerr rotation measurement with a lock-in amplifier.

The device was studied in a liquid-helium cooled cryostat with a sample temperature confirmed by the peak energy shift in photoluminescence and reflectance measurements.[16,17] Figure 2a shows the reflection contrast spectrum, $\Delta R/R$, of the sample at room temperature and at 20 K. The blueshift and narrowing of both the A and B (higher energy) peaks can be seen in the data. In the inset, we fit the A exciton peak in the $\Delta R/R$ spectrum, differentiated with respect to photon energy E, to a dielectric function of the form

$$\varepsilon(E) = \varepsilon_b + \sum_i \frac{f_i}{E_{0i}^2 - E^2 - iE\gamma_i} \quad (1)$$

Here f_i, E_{0i}, and γ_i are the oscillator strength, resonance energy, and line width of the ith transition, and ε_b is a nonresonant background contribution to the dielectric function. For our device at V_{GS} = 0 V and 20 K, we find that we can describe the A-exciton feature with an oscillator strength of f_A = 1.37 eV^2, an energy of E_{0A} = 1.75 eV, and a line width of γ_A = 28.9 meV. We assume an effective layer thickness of 0.649 nm.[18]

Figure 2b shows $\Delta R/R$ spectra as we vary the back-gate voltage. We deduced that our sample is intrinsically n-doped as a higher negative gate-bias is required to observe the positively charged exciton (trion) feature. This asymmetry, arising from unintentional n-doping of the sample, is also reflected in the electrical characteristics of the device presented in Figure 3a,b. The peak around 1.75 eV corresponds to the A exciton resonance and the lower-energy peaks arise from p- and n-doped trions in the highly gated regimes. We fit the reflection contrast derivative for gate voltages of 0 V, −10 V, and −20 V and the resulting parameters for A exciton and p-trion are shown in Figure S2 in Supporting Information Section S3. We use a simple capacitor model, described in the next section, to estimate the associated charge density. If we set the point of charge neutrality to −10 V, we find that the A exciton oscillator strength is reduced by 17% by increasing the gate voltage from −10 V to −20 V. Extrapolating linearly, the exciton absorption should disappear at $V_{GS} \approx -70$ V or a charge density of $p_0 \approx 10^{13}$ cm^{-2}. This behavior agrees with that previously reported for electrons in monolayer WS_2 on a SiO_2/Si substrate,[19] although a stronger variation of the optical properties with charge density was observed for TMDC monolayers encapsulated in h-BN.[20]

We use the measured doping dependence of the exciton strength to model the expected KR as a function of the valley

DOI: 10.1021/acs.nanolett.8b03838
Nano Lett. 2019, 19, 770−774

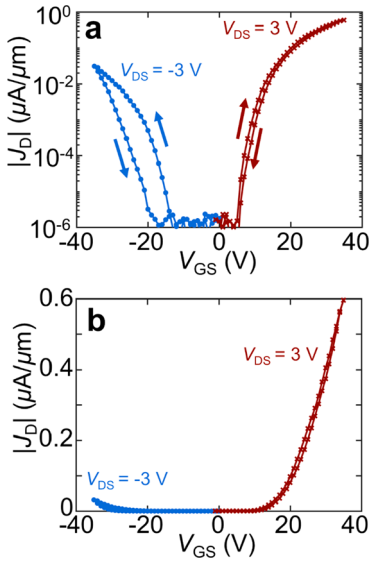

Figure 3. Drain current J_D as a function of back-gate voltage V_{GS} of the device at 20 K for $V_{DS} = -3$ and 3 V plotted with (a) logarithmic and (b) linear vertical scales. The arrows represent the direction of the voltage sweep. From these data, we infer threshold voltages of $V_T \approx -20\ V$ (p-doped) and $V_T \approx 15\ V$ (n-doped).

carrier imbalance. For each valley, we assume that the corresponding exciton loses all its oscillator strength for a charge density of 5×10^{12} cm^{-2}. Taking into account the relevant optical propagation effects in our device structure, as discussed in the Supporting Information Section S4, we find that the resulting valley imbalance in the valence band per unit Kerr rotation is $s_\theta = \frac{\Delta p}{\Delta \theta_K} = 6.7 \times 10^7$ cm^{-2}/μrad for probing at 700 nm, where $\Delta p = p^\uparrow - p^\downarrow$ is difference in the (sheet) concentrations of spin up and spin down carriers. This conversion factor incorporates contributions from both the real and imaginary parts of the dielectric function of the TMDC layer, which are coupled to polarization rotation of the probe optical field for the multilayered substrate.

In the case of electron doping, we obtained a stronger KR signal on the low-energy side of the A exciton. A KR would result from trion contributions to the optical response,[21−23] as discussed in Supporting Information Section S4. We expect that the main contribution at the probe wavelength would be from the lower energy n-type trion.

Electrical Characterization. The device current versus gate voltage (J_D versus V_{GS}) characteristics are presented in Figures 3a,b for $V_{DS} = \pm 3$ V DC. These data were obtained with approximately the RMS ac voltage applied during the KR measurements, with the same source contact grounded for both the electrical and optical measurements. The reverse bias data (not shown) exhibit weaker current flow. Additional electrical plots are included in Supporting Information Section S5. From these data, we estimate carrier concentrations using a parallel plate capacitor model, $n = C_{ox}(V_{GS} - V_T)/e$, where n is the concentration of electrons or holes, e is the elementary charge, $C_{ox} \approx 34.5$ nF/cm^2 is the oxide capacitance (per unit area), and V_T is the threshold voltage.[24] At $V_{GS} = -30$ and 30 V, we found $p_0 = (2 \pm 1) \times 10^{12}$ cm^{-2} in the p-regime and $n_0 = (3 \pm 1) \times 10^{12}$ cm^{-2} in the n-regime, where the error comes from uncertainty in V_T. From the near-linear regime of the J_D versus V_{GS} response, we use the transconductance to estimate the field-effect mobility[25] of the channel at 20 K. We find mobilities of $\mu = 0.11 \pm 0.07$ cm^2/(V s) for the p-regime and $\mu = 0.81 \pm 0.06$ cm^2/(V s) for the n-regime. The measured values are 2 orders of magnitude smaller than previous statistical TMDC mobility measurements[26] and two or more orders of magnitude smaller than the highest mobilities measured in WSe_2.[27,28] The lower apparent mobilities in our samples reflect an underestimate of the true values because of the role of contact resistance in our simple two-terminal measurements. In addition, our devices lack the channel encapsulation typically used to achieve high conductivities.

Kerr Rotation Scans. Representative line scans of the KR (θ_K) moving across the channel in the transverse ($\hat{x}$) direction are shown in Figure 4 for both the p-doped ($V_{GS} = -30$ V) and

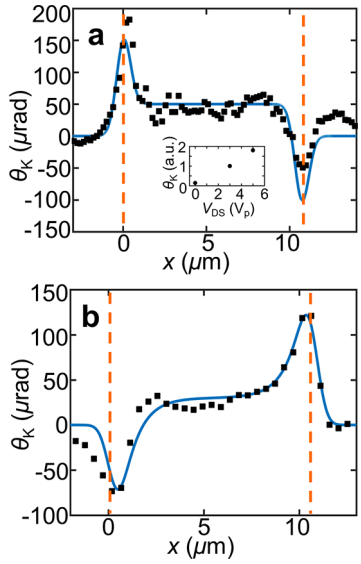

Figure 4. Kerr rotation scans across the channel compared with results of the drift-diffusion model for (a) the p-doped regime ($V_{GS} = -30$ V) probed using a 700 nm (1.77 eV) laser and (b) the *n*-doped regime ($V_{GS} = +30$ V) probed using a 730 nm (1.70 eV) laser. The experimental KR data are shown as black dots; the results of the model as blue lines. The inset of (a) shows the KR near the edge for increasing source-drain bias (measured at 730 nm), V_{DS} for $V_{GS} = -20$ V. The dashed lines mark edges of the channel. The measurements were performed at 20 K with $V_{DS} = 5\ V_p$ (AC).

the n-doped ($V_{GS} = 30$ V) regimes. On the bare substrate, there is no meaningful KR. We see distinct peaks of θ_K of opposite sign on the two sides of the WSe_2 channel. We attribute this effect to the accumulation of carriers with opposite valley (and spin) on the edges of sample as the result of the deflection of the carriers from the VHE. The peaks of KR, θ_K, are slightly asymmetric. There is a slight offset in the center of the channel, which we ascribe to a magnetoelectric effect associated with unintentional strain in the sample.[29]

The measured KR in Figure 4a,b is responsive to the in-plane bias voltage, showing greater θ_K for greater V_{DS}, doubling from 3 V_p to 5 V_p and disappearing for $V_{DS} = 0$ (Figure 4a inset). We have also recorded θ_K as a function of V_{GS} and seen a positive correlation, as discussed in Supporting Information Section S6. The scans for p- and n-doped samples were taken with a 700 nm (1.77 eV) and 730 nm (1.70 eV) laser, respectively. We chose the wavelengths for each doping regime in order to optimize the signal and minimize photodoping induced by the laser. The focused laser spot had a diameter of 1 μm full width at half-maximum (fwhm).

DOI: 10.1021/acs.nanolett.8b03838
Nano Lett. 2019, 19, 770−774

Modeling of Results and Discussion. The experimental results of Figure 4a,b show the expected presence of opposite spin-valley polarization at the two edges of the channel. To analyze the results more quantitatively, we consider a spin drift-diffusion model for carrier transport under an applied in-plane electric field E. This approach has been used previously to explain the behavior of spin accumulation in GaAs.[30] Because the carrier spin is coupled to valley, we will refer to the carriers with spin-valley characteristics simply as spins in this section.

In steady state, the drift-diffusion model can be solved in closed form for reflecting boundaries and a channel sufficiently wide that the spin accumulation regions on the two edges do not overlap. The spatial distribution of the excess spin density, $s(x)$, across the channel is then given by

$$s(x) = p^{\uparrow} - p^{\downarrow} = \left(\frac{S}{l_D}\right)\left(e^{-x/l_D} - e^{(x-w)/l_D}\right) \tag{2}$$

where w is the width of the channel, l_D is the spin diffusion length, and S is the integrated spin density (per unit length) along either edge. The parameter S can be written in terms of the spin-lifetime τ_s as

$$S = \tau_s \frac{\sigma_s}{\sigma_c}\frac{J_D}{e} = \tau_s \frac{\sigma_s}{e} E \tag{3}$$

where σ_s is the spin-valley Hall conductivity and σ_c is the charge (sheet) conductivity. We can approximate the spin diffusion length as $l_D = \sqrt{D\tau_s}$, where the D is the carrier diffusivity, which can, in turn, be related to the carrier mobility through the Einstein relationship.

Our experimental KR traces exhibit peaks at the channel edges with width consistent with the Gaussian laser beam profile. This implies that under our experimental conditions l_D is much smaller than the laser spot size.

By integrating the experimental KR profile, we can obtain an estimate of the spin accumulation S. In particular, using our inferred value for the relation between intervalley hole density difference and KR, $s_\theta = 6.7 \times 10^7$ cm^{-2}/μrad, from Figure 4a we obtain an experimental spin accumulation of $S = 44$ μm^{-1} in the p-doped regime. Here we have taken the average of the integrals of the two peaks, subtracting out the uniform background signal present over the sample. To compare S with two-dimensional spin densities, we can write $S = 4.4 \times 10^9$ (spins/cm^2)μm, that is, over a width of 1 μm near the edge of the sample, the average excess spin density is 4.4×10^9 cm^{-2}.

Within the drift-diffusion model, we can relate the experimental integrated excess spin obtained to material properties through eq 3. In particular, we make use of our experimental result to estimate the spin lifetime $\tau_s = S\frac{\sigma_c}{\sigma_s}\frac{e}{J_D}$.

To do so, we first determine the current density in our experiment for a dc measurement with $V_{DS} = 3$ V (dc), comparable to our RMS voltage in the KR measurements. We find from Figure 3 a value of $J_c = 10^{-2}$ μA/μm, based on the average value of the swept scan of the gate voltage at the relevant gate voltage of $V_{GS} = -30$ V. The spin conductivity is taken as $\sigma_s = 1.3 \times 10^{-3}$ $e^2/\hbar$ for $p_0 = 10^{13}$ cm^{-2}, as predicted by first principle calculations for TMDC monolayers[7] and scaled linearly for the carrier concentration in our sample. Using the hole mobility inferred above from the measured electrical characteristics, we find $\sigma_c = \mu e p_0 = 35$ nS. With these parameters, we then obtain $\tau_s = 0.4$ ns, a value at the lower end of the range of previously determined spin-polarized hole lifetimes.[12,31−33] Since we are likely underestimating σ_c, we can consider this a lower bound for τ_s.

With an estimate for τ_s in hand, we can use $l_D = \sqrt{D\tau_S}$ to infer a lower bound for the spin diffusion length of 3 nm. This is consistent with our earlier experimental observation that the diffusion length should be much shorter than the laser spot size (1 μm). In a pristine sample with mobilities around 100 cm^2/(V s) and valley-polarized lifetimes of 100 ns, we expect diffusion lengths on the order of 1 μm.

The solid lines in Figure 4a,b show the result of the drift-diffusion model, eq 2, using the experimentally deduced parameters, including a constant offset over the sample and convolution with the 1 μm fwhm Gaussian laser spatial profile.

Our estimate of the spin diffusion length also allows us to evaluate the degree of spin polarization near the edges. For the lower bound $l_D = 3$ nm, we infer approximately 70% spin polarization, $\frac{S/l_D}{p_0}$, under our experimental conditions. For a longer assumed spin diffusion length of, for example, 100 nm, we would infer from our experimental KR results a spin-valley polarization for holes of 2% at the edge of the sample.

For the n-doped regime, we are also able to fit the peaks in the KR scans to a diffusion length of $l_D < 1$ μm. In view of the uncertainties in deducing spin-valley densities from the experimental KR values for the n-doped regime, as discussed above, we have not attempted to analyze quantitatively the magnitude of the measured KR.

In the KR scans for both p- and n-doping, the left peak exhibits a slightly sharper decay than the right peak. We believe that this effect is a scanning artifact, reflecting either a decrease in the channel current after applying a gate bias at the start of the scan or the presence of n-type photodoping as observed in the electrical characteristics and discussed in Supporting Information Sect. S5. In either case, changes should be more significant near the start (left-side) of the scan.

In conclusion, we have investigated the VHE in WSe_2 monolayer transistors under current flow for both electron and hole doping by spatially mapping the spin-valley polarization across the channel using the optical Kerr effect. The spatial distribution and magnitude of the spin accumulation agree with a drift-diffusion transport model with reasonable material parameters. In the p-regime, we deduce a spin accumulation of 44 spins/μm and infer a lower bound of 0.4 ns for the spin lifetime. Because there have been reports of spin lifetimes on the order of 1 μs,[12,33] much greater spin accumulations and spin-diffusion lengths should be attainable using improved samples and sample environment. We have shown electrical control of the doping and the spin accumulation from the VHE, and we have observed for the first time the VHE in the p-doped regime. As the valence band spin-splitting greatly exceeds thermal energies at room temperature, studies of the VHE in p-doped samples at higher temperatures are warranted.

■ ASSOCIATED CONTENT

Supporting Information

The Supporting Information is available free of charge on the ACS Publications website at DOI: 10.1021/acs.nanolett.8b03838.

DOI: 10.1021/acs.nanolett.8b03838
Nano Lett. 2019, 19, 770−774

Measurement setup, sample fabrication, modeling of reflection contrast, analysis of KR to the valley carrier imbalance, electrical characterization, and the doping dependence of KR (PDF)

AUTHOR INFORMATION

Corresponding Author

*E-mail: tony.heinz@stanford.edu.

ORCID

Elyse Barré: 0000-0003-2119-0707

Connor J. McClellan: 0000-0002-8733-9968

Eric Pop: 0000-0003-0436-8534

Author Contributions

E.B. and J.A.C.-I. conceived and carried out the device fabrication and measurements. S.H.K. built the optical setup and assisted with experiments. C.M. assisted with experiments and analysis. E.P., H.-S.P.W., and T.F.H. supervised the work. All authors contributed to the analysis and interpretation of results and preparation of the manuscript.

Funding

The Kerr rotation measurements were supported by Air Force Office of Scientific Research (AFOSR) Grant FA9550-14-1-0040 and optical characterization by the Gordon and Betty Moore Foundation's EPiQS program through Grant GBMF4545 and the National Science Foundation (NSF) newLAW program (award 1741691). The electrical measurements were supported by the NSF 2-DARE EFRI program (award 1523883) and by AFOSR Grant FA9550-14-0251. Device fabrication was performed in the nano@Stanford laboratories, supported by the NSF as part of the National Nanotechnology Coordinated Infrastructure under award ECCS-1542152, and the Stanford Nano Shared Facilities (SNSF), supported by the NSF under award ECCS-154215. J.A.C-I. acknowledges support from the Center for Energy Efficient Electronics Science (NSF award 0939514). E.B. acknowledges support from the Natural Sciences and Engineering Research Council (NSERC) of Canada through a PGS-D fellowship (PGSD3-502559-2017).

Notes

The authors declare no competing financial interest.

ACKNOWLEDGMENTS

We would like to thank Dr. Ralph H. Page for editorial comments.

REFERENCES

(1) Raja, A.; Montoya Castillo, A.; Zultak, J.; Zhang, X.-X.; Ye, Z.; Roquelet, C.; Chenet, D. A.; van der Zande, A. M.; Huang, P.; Jockusch, S.; et al. *Nano Lett.* **2016**, *16*, 2328−2333.

(2) Xiong, F.; Wang, H.; Liu, X.; Sun, J.; Brongersma, M.; Pop, E.; Cui, Y. *Nano Lett.* **2015**, *15*, 6777−6784.

(3) English, C. D.; Shine, G.; Dorgan, V. E.; Saraswat, K. C.; Pop, E. *Nano Lett.* **2016**, *16*, 3824−3830.

(4) Liu, W.; Kang, J.; Cao, W.; Sarkar, D.; Khatami, Y.; Jena, D.; Banerjee, K. *Electron Devices Meet. (IEDM), 2013 IEEE Int.* **2013**, 14−19.

(5) Mak, K. F.; McGill, K. L.; Park, J.; McEuen, P. L. *Science (Washington, DC, U. S.)* **2014**, *344*, 1489−1492.

(6) Xiao, D.; Liu, G.-B. B.; Feng, W.; Xu, X.; Yao, W. *Phys. Rev. Lett.* **2012**, *108*, 196802.

(7) Feng, W.; Yao, Y.; Zhu, W.; Zhou, J.; Yao, W.; Xiao, D. *Phys. Rev. B: Condens. Matter Mater. Phys.* **2012**, *86*, 165108.

(8) Lee, J.; Mak, K. F.; Shan, J. *Nat. Nanotechnol.* **2016**, *11*, 421−425.

(9) Zhu, Z. Y.; Cheng, Y. C.; Schwingenschlögl, U. *Phys. Rev. B: Condens. Matter Mater. Phys.* **2011**, *84*, 153402.

(10) Zhang, X. X.; Cao, T.; Lu, Z.; Lin, Y. C.; Zhang, F.; Wang, Y.; Li, Z.; Hone, J. C.; Robinson, J. A.; Smirnov, D.; et al. *Nat. Nanotechnol.* **2017**, *12*, 883−888.

(11) Le, D.; Barinov, A.; Preciado, E.; Isarraraz, M.; Tanabe, I.; Komesu, T.; Troha, C.; Bartels, L.; Rahman, T. S.; Dowben, P. A. *J. Phys.: Condens. Matter* **2015**, *27*, 182201.

(12) Dey, P.; Yang, L.; Robert, C.; Wang, G.; Urbaszek, B.; Marie, X.; Crooker, S. A. *Phys. Rev. Lett.* **2017**, *119*, 137401.

(13) Zhou, B. T.; Taguchi, K.; Kawaguchi, Y.; Tanaka, Y.; Law, K. T. ArXiV Prepr. 1712.02942 **2017**.

(14) Yao, W.; Xiao, D.; Niu, Q. *Phys. Rev. B: Condens. Matter Mater. Phys.* **2008**, *77*, 235406.

(15) Mak, K. F.; He, K.; Shan, J.; Heinz, T. F. *Nat. Nanotechnol.* **2012**, *7*, 494−498.

(16) Zhu, C. R.; Zhang, K.; Glazov, M.; Urbaszek, B.; Amand, T.; Ji, Z. W.; Liu, B. L.; Marie, X. *Phys. Rev. B: Condens. Matter Mater. Phys.* **2014**, *90*, 161302.

(17) Arora, A.; Koperski, M.; Nogajewski, K.; Marcus, J.; Faugeras, C.; Potemski, M. *Nanoscale* **2015**, *7*, 10421−10429.

(18) Wilson, J. A.; Yoffe, A. D. *Adv. Phys.* **1969**, *18*, 193−335.

(19) Chernikov, A.; van der Zande, A. M.; Hill, H. M.; Rigosi, A. F.; Velauthapillai, A.; Hone, J.; Heinz, T. F. *Phys. Rev. Lett.* **2015**, *115*, 126802.

(20) Wang, Z.; Zhao, L.; Mak, K. F.; Shan, J. *Nano Lett.* **2017**, *17*, 740−746.

(21) Courtade, E.; Semina, M.; Manca, M.; Glazov, M. M.; Robert, C.; Cadiz, F.; Wang, G.; Taniguchi, T.; Watanabe, K.; Pierre, M.; et al. *Phys. Rev. B: Condens. Matter Mater. Phys.* **2017**, *96*, 085302.

(22) Yu, H.; Liu, G. B.; Gong, P.; Xu, X.; Yao, W. *Nat. Commun.* **2014**, *5*, 3876.

(23) Jones, A. M.; Yu, H.; Ghimire, N. J.; Wu, S.; Aivazian, G.; Ross, J. S.; Zhao, B.; Yan, J.; Mandrus, D. G.; Xiao, D.; et al. *Nat. Nanotechnol.* **2013**, *8*, 634−638.

(24) Datye, I. M.; Gabourie, A. J.; English, C. D.; Smithe, K. K. H.; McClellan, C. J.; Wang, N. C.; Pop, E. *2D Mater.* **2019**, *6*, 011004.

(25) Fuhrer, M. S.; Hone, J. *Nat. Nanotechnol.* **2013**, *8*, 146−147.

(26) Smithe, K. K. H.; Suryavanshi, S. V.; Muñoz Rojo, M.; Tedjarati, A. D.; Pop, E. *ACS Nano* **2017**, *11*, 8456−8463.

(27) Chuang, H.-J.; Tan, X.; Ghimire, N. J.; Perera, M. M.; Chamlagain, B.; Cheng, M. M.-C.; Yan, J.; Mandrus, D.; Tománek, D.; Zhou, Z. *Nano Lett.* **2014**, *14*, 3594−3601.

(28) Cai, L.; McClellan, C. J.; Koh, A. L.; Li, H.; Yalon, E.; Pop, E.; Zheng, X. *Nano Lett.* **2017**, *17*, 3854−3861.

(29) Lee, J.; Wang, Z.; Xie, H.; Mak, K. F.; Shan, J. *Nat. Mater.* **2017**, *16*, 887−891.

(30) Stern, N. P.; Steuerman, D. W.; Mack, S.; Gossard, A. C.; Awschalom, D. D. *Appl. Phys. Lett.* **2007**, *91*, 062109.

(31) Hsu, W.-T.; Chen, Y.-L.; Chen, C.-H.; Liu, P.-S.; Hou, T.-H.; Li, L.-J.; Chang, W.-H. *Nat. Commun.* **2015**, *6*, 8963.

(32) Song, X.; Xie, S.; Kang, K.; Park, J.; Sih, V. *Nano Lett.* **2016**, *16*, 5010−5014.

(33) Kim, J.; Jin, C.; Chen, B.; Cai, H.; Zhao, T.; Lee, P.; Kahn, S.; Watanabe, K.; Taniguchi, T.; Tongay, S.; et al. *Sci. Adv.* **2017**, *3*, No. e1700518.

DOI: 10.1021/acs.nanolett.8b03838
Nano Lett. 2019, 19, 770−774

Supporting Information: **Spatial Separation of Carrier Spin by the Valley Hall Effect in Monolayer WSe_2 Transistors**

Elyse Barré [1], Jean Anne C. Incorvia[1,2], Suk Hyun Kim[3], Connor J. McClellan[1], Eric Pop[1,4], H.-S. Philip Wong[1], and Tony F. Heinz[3,5]*

[1]Dept. of Electrical Engineering, Stanford University, Stanford, California 94305, U.S.A.

[2]Dept. of Electrical and Computer Engineering, University of Texas at Austin, Austin, Texas 78712, U.S.A.

[3]Depts. of Applied Physics and Photon Science, Stanford University, Stanford, California 94305, U.S.A.

[4]Department of Materials Science and Engineering, Stanford University, Stanford, California 94305, U.S.A

[5]SLAC National Accelerator Laboratory, Menlo Park, California 94025, U.S.A

*Corresponding author: tony.heinz@stanford.edu

S1. Experimental set-up for Kerr rotation measurements

The optical source for the Kerr rotation (KR) measurements was a supercontinuum laser (Fianium WhiteLase supercontinuum lasers, NKT Photonics). The wavelength was selected using a bandpass filter (10 nm FWHM) such that it was be nearly resonant to the A exciton energy of the WSe_2 sample (~1.75 eV). This probe beam was linearly polarized and focused on the sample with a 40× objective lens. The spot size on the sample of ~1 μm FWHM was found by analyzing the image of the beam from the microscope camera.

Detection of the KR was accomplished using an optical bridge technique in which the reflected probe beam was passed through a Wollaston prism oriented at 45° with respect to the polarization of the unperturbed beam. The intensities of the two resulting orthogonally polarized beams were monitored by

separate photodiodes. The intensity difference is proportional to the KR (for the relevant regime of small KR). The difference signal from the photodiodes, after amplification, was detected by a lock-in amplifier synchronized with the AC source-drain voltage V_{DS} applied to the WSe_2 sample. Frequencies for V_{DS} in the range of 200 - 800 Hz were chosen to approximate the device behavior under DC bias conditions, while still maintaining favorable noise characteristics for the measurements. To calibrate the amplitude of signal from the lock-in amplified, we chopped the probe beam and measured the response produced by the signal of just one photodiode.

S2. Sample and device fabrication

We prepared the WSe_2 field-effect transistors using mechanical exfoliation, electron-beam lithography, and electron-beam evaporation. WSe_2 crystals from HQ Graphene were exfoliated onto polydimethylsiloxane (PDMS). After identifying monolayers using Raman spectroscopy and photoluminescence measurements, the selected flake was transferred onto the Si/SiO_2 substrate by heating to 40° C during transfer. The Si substrate was n^+ type, < 0.005 Ω-cm, <100> Si with 100(±5%) nm of SiO_2 from University Wafers. The samples were then annealed at 2×10^{-5} Torr and 250 ºC for 2 hours to reduce induced strain.

The flakes were patterned using polymethyl methacrylate (PMMA) electron-beam resist and electron-beam lithography, followed by etching with XFe_2. The PMMA was removed with acetone. Subsequent PMMA/electron-beam lithography steps were used to place the 30-nm Pd contacts and 2-nm Ti, 30-nm Pd contact pads using electron-beam evaporation. Pd was chosen for the contacts because its large work function (~5 eV) is suitable for *p*-type contacts and because its low evaporation temperature limits sample damage. After device fabrication, we again performed a high vacuum anneal at 2×10^{-5} Torr and 250 ºC for one hour to remove PMMA residue. Then the device was transferred to a second cryostat, temporarily breaking vacuum.

S3. Modeling of the WSe_2 reflection contrast spectra for different gate voltages

In this section, we analyze our measurements of reflection contrast spectra from the WSe_2 monolayer as a function of the gate voltage V_{GS} in order to determine how the material's optical response is affected by carrier density. In particular, we make use of the reflection contrast spectra presented in Fig. 2b of the main text for various gate voltages to determine the carrier-induced changes in the resonant energies, oscillator strengths, and line widths associated with the neutral and charged A exciton features in the dielectric function.

The reflection contrast, $\frac{\Delta R}{R}$, is defined as difference between reflectivity of the supported WSe_2 monolayer (R_{WSe2}) and that of the substrate SiO_2/Si (R_{SiO2}), normalized by the substrate reflectivity:

$$\frac{\Delta R}{R} = \frac{R_{WSe2} - R_{SiO2}}{R_{SiO2}} \quad \text{(S-1)}$$

These reflectivities and the structure that we measure are shown in Fig. S1a.

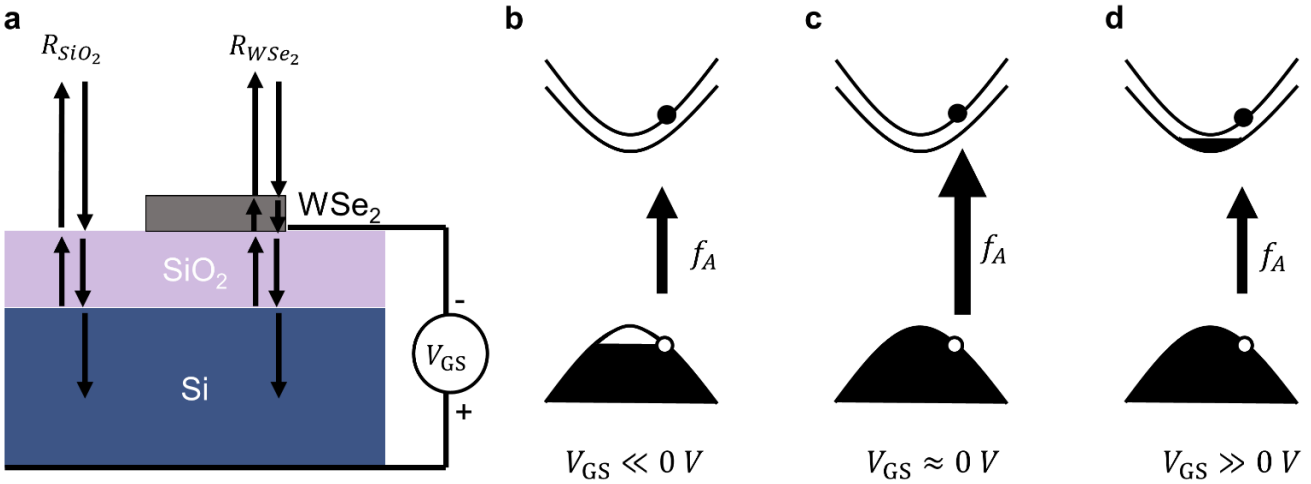

Figure S1. (a) Structure used for transfer matrix model of the optical response of the WSe_2 monolayer with an applied gate voltage. The sample is supported by a 100-nm SiO_2 gate dielectric and an underlying doped Si wafer. (b-d) An illustration of the band filling for the K or K' valley with the relative A exciton oscillator strength, f_A, shown by the arrow size for (b) a *p*-doped sample (c) a neutral sample (d) an *n*-doped sample.

Following previous treatments,[1] we model the variation of the WSe_2 dielectric function $\varepsilon(E)$ with photon energy E using Lorentzian contributions from transitions of neutral and charged excitons (trions), together with a constant real background, ε_b, from higher-lying transitions:

$$\varepsilon(E) = \varepsilon_b + \frac{f_A}{E_{0A}^2 - E^2 - iE\gamma_A} + \frac{f_T}{E_{0T}^2 - E^2 - iE\gamma_T} \quad \text{(S-2)}$$

Here E_{0i}, f_i and γ_i denote the resonant energy, oscillator strength, and line width of the neutral exciton (A) and trion (T). We ascribe a nominal thickness of 6.49 Å to the monolayer, corresponding to the bulk interlayer spacing. At higher *n*- or *p*-doping, we expect that the trion will have a greater oscillator strength and the exciton will be correspondingly weaker. This relationship is shown schematically in Figs. S1b-d.

We determine the parameters in the dielectric function of eq. (S-2) as a function of the gate voltage V_{GS} by fitting the corresponding reflection contrast spectrum (Fig. 2b). We do so by solving the optical wave propagation problem for the monolayer supported by the 100-nm SiO_2 gate dielectric and the bulk Si

substrate using the transfer matrix method.[2] The resulting fits to the energy derivatives of the reflection contrast spectra for V_{GS} = 0 V, -10 V, -20 V are presented in Fig. S2, as are the corresponding parameters for A exciton and contributions to the WSe_2 dielectric function.

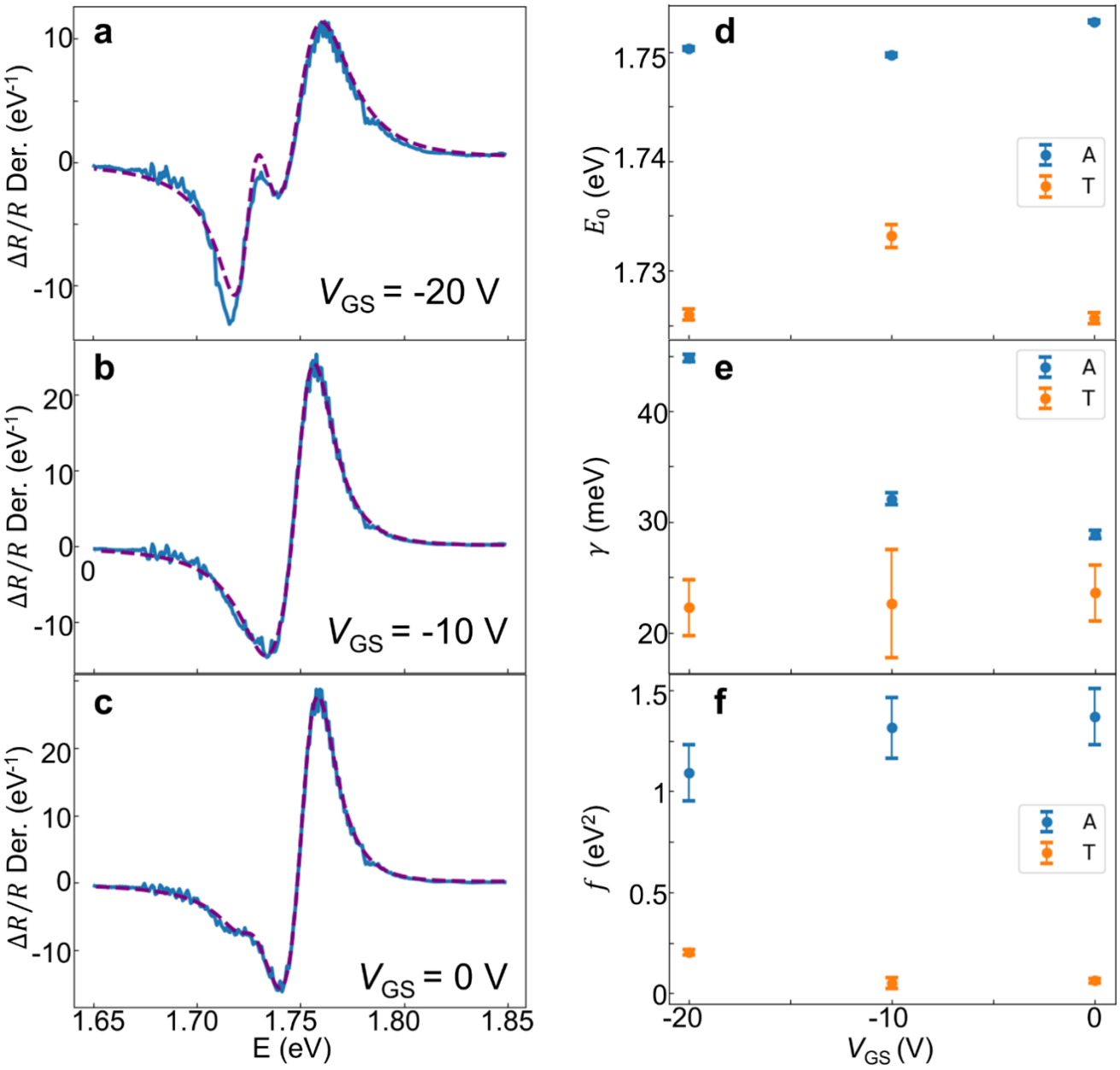

Figure S2. The energy derivative of the experimental reflection contrast spectra (solid blue) and fits (dashed purple) based on the treatment described in the text for gate voltages V_{GS} of (a) -20 V, (b) -10 V. and (c) 0 V. The corresponding values inferred for the (d) resonance energy, E_0, (e) line width, γ, and (f) oscillator strength, f, for the neutral exciton (A, in blue) and the charged exciton (T, in orange).

From the optical spectra, we infer a point of charge neutrality for the WSe_2 monolayer near V_{GS} = -10 V. We further observe a 17% reduction in the neutral exciton oscillator strength, f_A, for hole doping when changing V_{GS} from -10 V to -20 V. Applying linear extrapolation of this trend, we would expect that hole doping should fully suppress the neutral exciton feature for V_{GS} = -70 V, corresponding to a hole density of $p_0 \approx 10^{13}$ cm^{-2}. (This result is compatible with the observations of Ref. 3 for electron doping in WS_2.) We apply our finding on the influence of doping on the observed A exciton oscillator strength below to model the expected Kerr rotation for a given imbalance of the spin-valley carrier density.

S4. Modeling of Kerr rotation as a function of the imbalance in valley carrier density

Optical transitions contributing to the Kerr rotation under an imbalance in valley carrier density

In this section, we discuss contributions to the KR in different doping regimes. In the *p*-regime, when probing near the neutral A exciton, the Kerr rotation can be attributed to the difference in absorption of circularly polarized light (σ+ /σ-) by the bright, neutral A exciton arising from differences in population of the upper valence band, Δp, a shown in Fig. S3a. The valley imbalance would correspond to an opposite shift in both the real and imaginary parts of the dielectric function for σ+ /σ- polarized light around the bright neutral exciton.

In the *n*-regime, we found a more reliable signal in probing at a photon energy slightly below the trion resonance. Thus, we attribute our measured KR primarily to the trion response. The trion, like the exciton, has a Lorentzian line shape and a valley imbalance would correspond to an opposite shift in the real and imaginary parts of the σ+ and σ- dielectric function, respectively. In the *n*-doped regime, we must consider both the intravalley and the intervalley trion configuratitons.[4,5] Since we are probing with lower energy photons, below the intravalley trion transition, we expect a stronger contribution from the intravalley trion, which should have a lower transition energy.[6] We show the bright A exciton transition in the strongly *n*-doped regime in Fig. S3b, as well as the intravalley and intervalley *n*-type trions in Figs. S3c and S3d. Because of the complexity of influence of the intervalley charge imbalance on the KR in the *n*-doped regime, we do not attempt to analyze this relationship quantitatively, as we do below for the *p*-doped regime.

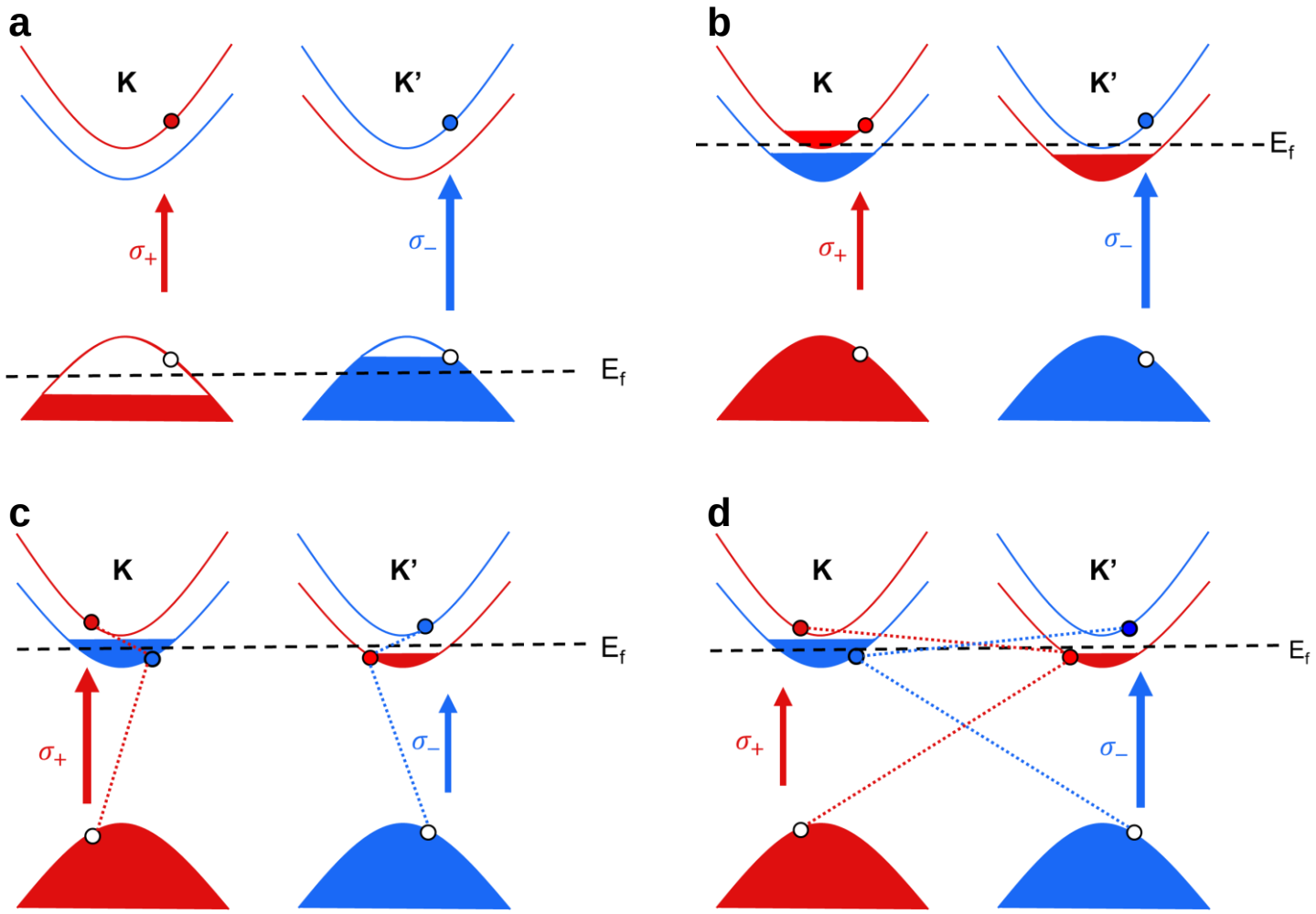

Figure S3. Mechanisms for coupling of the exciton resonances to the intervalley carrier imbalance for: (a) a *p*-doped sample where the neutral exciton transition has a stronger transition in the slightly more populated K' valley; (b) an *n*-doped sample under heavy doping where the neutral exciton a stronger transition for the less doped K' valley; (c) an *n*-doped sample where the intravalley trion has a stronger transition in the more doped K valley; (d) an *n*-doped sample where the intervalley trion has a stronger transition in the less doped K' valley.

Conversion from Kerr rotation to the imbalance in valley carrier density

In this section, we make use of our experimentally based model of the WSe_2 dielectric function and its dependence on doping to determine the expected a Kerr rotation for a given valley carrier imbalance in the *p*-doped regime. We assume the change in the carrier concentration in the K valley is linearly related to the A exciton oscillator strength of σ+ light (and K' with σ- light). In analyzing the KR for doping with V_{GS} = -30 V, we take the A exciton transitions in the K and K' valleys to have the same the line width and

resonance energy as the measured values for V_{GS} = -20 V and further neglect any possible changes in these quantities induced by the slight valley population imbalance. We are thus ignoring the doping-induced broadening of the peak, the Burstein-Moss effects which may shift the peak[7], and the emergence of trion features. We expect these corrections to be small since the carrier densities are relatively low, and we are probing on the higher energy side of the A exciton resonance peak. To complete our model of the material response, we assume that the A exciton oscillator strength varies linearly with level of *p*-doping in a fashion determined by the measurements of the gate-dependent optical spectra presented in Supplementary Section S3.

The transfer matrix approach used in conjunction with the model above of the polarization dependent dielectric function to determine the expected KR in our experimental geometry (Fig. S4a). More specifically, the KR is calculated as $\theta_{\sigma+} - \theta_{\sigma-}$, where $r_{\sigma\pm}$ is the complex reflectivity for $\sigma \pm$ polarized light and $\theta_{\sigma\pm}$ is the associated phase. We note that the calculation fully accounts for the influence of the layered substrate. Figure S4b shows the resulting predicted photon-energy dependence (θ_K vs E) for a valley imbalance of $\Delta p = p^{\uparrow} - p^{\downarrow} \approx 2 \times 10^{11}$ cm^{-2} with a total hole density of $p_0 \approx 2 \times 10^{12}$ cm^{-2}. For the 1.77 eV probe photon energy used for the *p*-type measurements, we obtain conversion between Kerr rotation and valley imbalance of $s_\theta = \frac{\Delta p}{\Delta \theta_K} = 6.7\times10^7$ cm^{-2}/μrad.

For the experimentally relevant case of a 100-nm thick SiO_2 on a bulk Si substrate, the predicted KR near the exciton resonance exhibits a dispersive line shape, as shown in Fig. S4b. This behavior reflects the fact that optical phase shift induced by the sample in this experimental geometry is predominantly sensitive to the real part of the dielectric function of the WSe_2 monolayer. We observe, however, that for a 300-nm SiO_2 layer the predicted KR has an absorptive line shape, as well as a significantly smaller magnitude. The strong dependence of the KR of the same sample on different substrates is important to bear in mind for any quantitative analysis of the Kerr rotation, as well as for obtaining a strong and reliable experimental probe of the valley carrier imbalance.

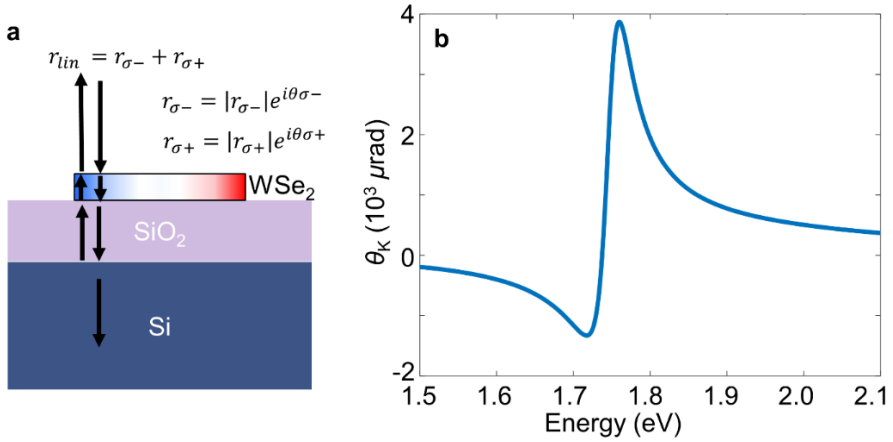

Figure S4. (a) Structure used for transfer matrix calculation of the optical response is a monolayer of WSe_2 with different values of dielectric function for $\sigma+/\sigma-$ light. as shown by colored gradient. (b) Predicted Kerr rotation from a *p*-doped sample with a valley charge imbalance of $\Delta p = p^{\uparrow} - p^{\downarrow} \approx 2 \times 10^{11}$ cm^{-2} and a total hole density of $p_0 \approx 2 \times 10^{12}$ cm^{-2}.

S5. Electrical measurements

In this section, we present additional results on the electrical characterization of our device and discuss the electrical properties of the sample that could affect our KR measurements. Figures S5a,b show the channel current J_D versus the gate voltage V_{GS} at temperatures of 20 K and 290 K, respectively. These measurements were performed a few days before the sample was optically characterized; the electrical measurements in the main text were performed shortly after the Kerr rotation studies.

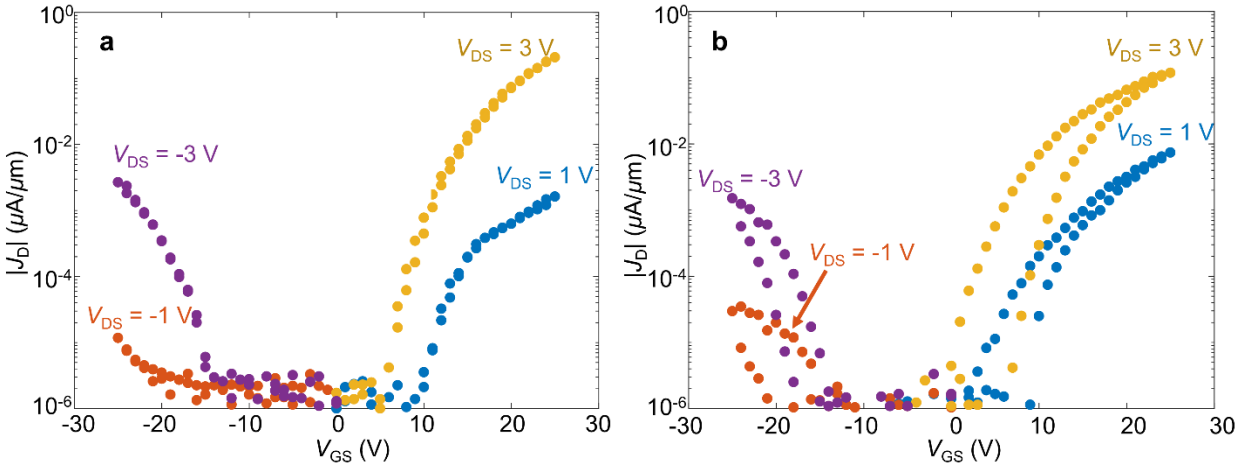

Figure S5. Drain current J_D versus gate voltage V_{GS} recorded before the Kerr rotation measurements at (a) 20 K and (b) 290 K for several values of channel bias V_{DS}, as shown by the different colored traces. Data for both upward and downward scans of the gate voltage are shown, with significant hysteresis seen in the measurements at 290 K.

At lower temperatures, there is reduced hysteresis and a greater turn-on voltage. If we have Schottky barriers at our contacts, lower temperature reduces thermionic emission over the barrier, thus requiring larger V_{GS} to turn on the channel.[8] The hysteresis observed in the electrical characterization was more pronounced in the *p*-regime, especially after completing the optical measurements (Fig. 3 of main text). During electrical measurements, we tested the effect of exposing the sample to the probe laser beam. For certain wavelengths, laser power exceeding 1 μW photodoped the sample into the *n*-type regime, so that the channel would conduct only for positive back-gate voltages. Thus, for Kerr rotation measurements with hole doping, we were particularly careful to use low probe laser powers.

S6. Variation in the Valley-Hall effect with level of hole doping

We have performed measurements of the VHE using the scans of the KR across the channel for different hole doping conditions. Here we present the measured KR induced in at the edges of the channel by the VHE as it evolves with changing gate voltage V_{GS}. We compare this behavior to the changes in drain current with gate voltage.

As we see from Fig. S6, θ_K increases significantly as the gate voltage is made more negative and the hole concentration increases. The channel current J_D also increases with hole concentration, as expected. While the variation of the channel current with gate voltage will reflect detailed characteristics of the contacts, it is natural to compare θ_K, as a measure of the VHE, with the longitudinal current J_D driving it. From Fig. S6, we see that while both θ_K and $|J_D|$ are positively correlated, the measured KR grows sub-linearly with $|J_D|$, in the case where we are manipulating the back-gate. From our analysis in the main text, we expect a spin-valley accumulation of $S = \tau_s \frac{\sigma_s}{\sigma_c} \frac{J_D}{e}$.

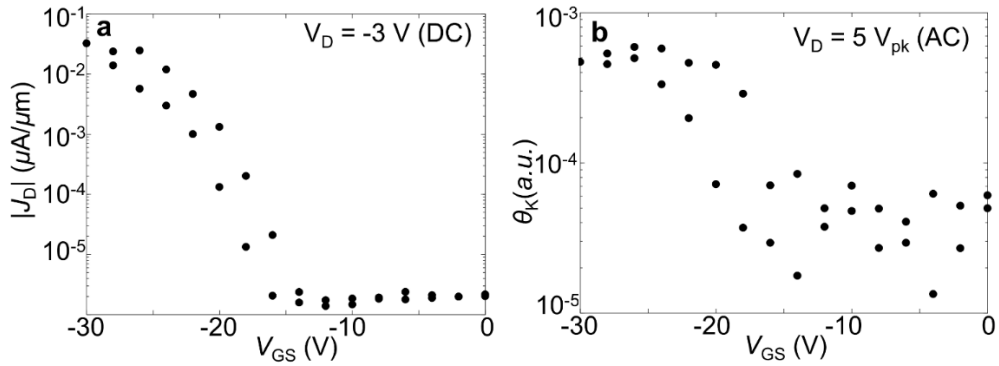

Figure S6. Comparing the current during DC and the KR due to the VHE. (a) Drain current $|J_D|$ versus gate voltage V_{GS}. (b) KR due to the VHE measured at the edge of the device versus gate voltage. Kerr rotation at the edge of the sample for the same range of gate voltages.

We might accordingly predict that θ_K should increase *linearly* with the channel current J_D, assuming, as above, that θ_K varies linearly with *S*.

On closer consideration, the lack of linear scaling of the spin-valley accumulation *S* (or θ_K) with the channel current J_D is not unexpected. In particular, linear variation of *S* with J_D assumes that the combination of parameters $\tau_s \frac{\sigma_s}{\sigma_c}$ is independent of hole density. Now in the simplest picture, we might expect both the charge conductivity $\sigma_c = ep_0\mu$ and the valley-Hall conductivity σ_s to grow linearly with carrier concentration, thus keeping their ratio fixed. However, for with increasing carrier concentration, p_0, defect screening[9] should, in fact, lead to an increase of the hole mobility μ and superlinear growth of σ_c with p_0. On the other hand, at least the intrinsic contribution to spin-valley conductivity σ_s is expected to grow linearly in p_0.[10] Thus, sub-linear scaling of S with J_D is would result. In addition, the spin-valley lifetime τ_s may vary with doping level. Finally, there may be deviations from the assumed linearity of the Kerr rotation, the experimentally measured quantity, with the underlying spin-valley imbalance *S* in the sample. In particular, trion transitions may contribute to s_θ with the opposite sign from the neutral exciton transitions, similar to the *n*-doped cases discussed above. This could lead to a variation in the value of s_θ with doping level.

References

(1) Li, Y.; Chernikov, A.; Zhang, X.; Rigosi, A.; Hill, H. M.; van der Zande, A. M.; Chenet, D. A.; Shih, E.-M.; Hone, J.; Heinz, T. F. *Phys. Rev. B* **2014**, *90*, 205422.

(2) Byrnes, S. J. *ArXiv* **2018**, *arXiv:1603*, 1–20.

(3) Chernikov, A.; van der Zande, A. M.; Hill, H. M.; Rigosi, A. F.; Velauthapillai, A.; Hone, J.; Heinz, T. F. *Phys Rev Lett* **2015**, *115*, 126802.

(4) Jones, A. M.; Yu, H.; Ghimire, N. J.; Wu, S.; Aivazian, G.; Ross, J. S.; Zhao, B.; Yan, J.; Mandrus, D. G.; Xiao, D.; et al. *Nat. Nanotechnol.* **2013**, *8*, 634–638.

(5) Courtade, E.; Semina, M.; Manca, M.; Glazov, M. M.; Robert, C.; Cadiz, F.; Wang, G.; Taniguchi, T.; Watanabe, K.; Pierre, M.; et al. *Phys. Rev. B* **2017**, *96*, 085302.

(6) Yu, H.; Liu, G. Bin; Gong, P.; Xu, X.; Yao, W. *Nat. Commun.* **2014**, *5*, 3876.

(7) Kim, J.; Jin, C.; Chen, B.; Cai, H.; Zhao, T.; Lee, P.; Kahn, S.; Watanabe, K.; Taniguchi, T.; Tongay, S.; et al. *Sci. Adv.* **2017**, *3*, e1700518.

(8) Lin, Y.-F.; Xu, Y.; Wang, S.-T.; Li, S.-L.; Yamamoto, M.; Aparecido-Ferreira, A.; Li, W.; Sun, H.; Nakaharai, S.; Jian, W.-B.; et al. *Adv. Mater.* **2014**, *26*, 3263–3269.

(9) Ma, N.; Jena, D. *Phys. Rev. X* **2014**, *4*, 011043.

(10) Xiao, D.; Liu, G.-B. B.; Feng, W.; Xu, X.; Yao, W. *Phys Rev Lett* **2012**, *108*, 196802.